MatP local enrichment delays segregation independently of tetramer formation and septal anchoring in *Vibrio cholerae*

Elena Espinosa[1], Jihane Challita[1], Jean-Michel Desfontaines[1], Christophe Possoz[1], Marie-Eve Val[2], Didier Mazel[2], Martial Marbouty[3], Romain Koszul[3], Elisa Galli[1*], and François-Xavier Barre[1*]

[1] Institute for Integrative Biology of the Cell (I2BC), Université Paris-Saclay, CEA, CNRS, Université Paris Sud, 1 Avenue de la Terrasse, 91198 Gif-sur-Yvette, France

[2] Institut Pasteur, Université Paris Cité, CNRS UMR3525, Unité Plasticité du Génome Bactérien, Paris 75015, France

[3] Institut Pasteur, Université Paris Cité, CNRS UMR3525, Unité Spatial Regulation of Genomes, Paris 75015, France

# These authors contributed equally: Elena Espinosa, Jihane Challita

* To whom correspondence should be addressed. Tel: +33 169 823 224; Email: elisa.galli@i2bc.paris-saclay.fr, francois-xavier.barre@i2bc.paris-saclay.fr

Abstract

Vibrio cholerae harbours a primary chromosome derived from the monochromosomal ancestor of the Vibrionales (ChrI) and a secondary chromosome derived from a megaplasmid (ChrII). The coordinated segregation of the replication terminus of both chromosomes (*TerI* and *TerII)* determines when and where cell division occurs. ChrI encodes a homolog of *Escherichia coli* MatP, a protein that binds to a DNA motif (*matS*) that is overrepresented in replication termini. Here, we use a combination of deep sequencing and fluorescence microscopy techniques to show that *V. cholerae* MatP structures TerI and TerII into macrodomains, targets them to mid-cell during replication, and delays their segregation, thus supporting that ChrII behaves as a bona fide chromosome. We further show that the extent of the segregation delay mediated by MatP depends on the number and local density of *matS* sites, and is independent of its assembly into tetramers and any interaction with the divisome, in contrast to what has been previously observed in *E. coli*.

Introduction

Chromosome segregation and cell division must be coordinated in space and time to ensure the faithful transmission of genetic information. In eukaryotes, this is achieved by linking several steps of cytokinesis to the assembly and activity of the mitotic spindle, the eukaryotic chromosome segregation machinery. In bacteria, which lack a functional equivalent of the mitotic spindle, the genomic DNA itself is involved in the regulation of cell division[1–3]. This has been remarkably illustrated in *Vibrio cholerae* - the causative agent of the deadly human diarrhoeal disease of the same name, in which the positioning and timing of assembly of the divisome is primarily dictated by the cellular arrangement and choreography of segregation of the chromosomes[4,5].

V. cholerae is a curved rod-shaped monotrichous bacterium (Fig. 1a). It is intrinsically polarised with a ‘new’ pole resulting from the division of the mother cell and an ‘old’ flagellated pole (Fig. 1a). Its genome is distributed on a primary chromosome derived from the monochromosomal ancestor of the Vibrionales (ChrI) and a secondary chromosome derived from a megaplasmid

(ChrII)[6]. ChrI and ChrII both carry a single origin of replication, *ori1* and *ori2*, with replication terminating in a diametrically opposite zone, *TerI* and *TerII*, which contains a site dedicated to the resolution of chromosome dimers by the XerCD/FtsK machinery, *dif1* and *dif2*, respectively (Fig. 1a and 1b)[7,8]. Both are arranged longitudinally in the cell, with *TerI* and *TerII* migrating from the new pole to mid-cell in the course of replication (Fig. 1a)[9,10]. Binding sites for a DNA-associated protein that inhibits divisome assembly, SlmA, are enriched all along ChrI and ChrII except for *TerI* and *TerII* (Fig. 1a)[1,4]. Thus, the positioning of *TerI* and *TerII* restricts septum formation to mid-cell at the end of the cell cycle (Fig. 1a)[4,5]. Accordingly, we observed cell division defects in MCH1, a synthetic monochromosomal strain in which all of ChrII except *ori2* and its partition machinery is inserted into ChrI at the *dif1* locus[4].

But what is the mechanism that drives the choreography of *TerI* and *TerII* segregation? ChrI encodes for a homolog of MatP, a protein that binds as a dimer to a DNA motif, *matS*, that is overrepresented in the replication terminus region of the *Escherichia coli* chromosome, *Ter* [11,12]. MatP plays two roles in *E. coli*: (i) it structures *Ter* into a macrodomain (MD) by limiting long-range *cis* contacts (*cis* contacts between DNA sequences separated by more than 280 kbp) between *Ter* and the rest of the genome[13,14] and (ii) it ensures the colocalisation of sister *Ter* copies at mid-cell until the onset of septation[15]. The last 20 carboxy-terminal amino acid residues of MatP induce the formation of tetramers (dimers of dimers) that can link *matS* sites to each other and/or to other DNA segments[12,16]. Tetramers are dispensable for MD formation [14]. Their role in the initial post-replicative pairing of sister *Ter* copies is still under debate[16,17]. However, the prolonged positioning of sister *Ter* copies at mid-cell is thought to be due to the interaction of the tetramerization domain with a cell division protein, ZapB[15,16,18,19]. Functional homologs of MatP and ZapB similarly link the *Ter* of the *Caulobacter crescentus* chromosome to the divisome[20,21]. Based on the *E. coli matS* motif consensus, 34 and 14 putative *matS* sites have been identified in *TerI* and *TerII*, respectively[13]. Early work showed that the deletion of *matP* led to the early separation of sister *dif1* loci and the erratic positioning of *dif2* loci[10], and impaired cell division[4]. However, sister *dif1* loci were found to remain associated independently of divisome assembly during the recovery of *V. cholerae* spheroplasts to a proliferative rod-

77 shaped state, contradicting the idea that MatP prolonged the colocalization of sister *TerI* copies
78 by tethering them to the divisome[22]. In addition, sister *dif2* loci were found to separate and
79 move away from mid-cell prior to sister *dif1* copies at the onset of constriction[10]. These
80 observations questioned the role and action mode of MatP in *V. cholerae*.
81 Here, we have used a combination of deep sequencing and fluorescence microscopy
82 techniques to investigate the role of MatP in *V. cholerae*. We show that it binds to a very large
83 number of sites in *TerI* and *TerII*, similar to but more diverse than the *E. coli matS* sites. We
84 also show that MatP structures *TerI* and *TerII* into macrodomains, targets them to mid-cell in
85 the course of replication and delays their segregation, demonstrating that ChrII is organised
86 and behaves as a *bona fide* chromosome. However, in contrast to what has been observed in
87 *E. coli*, we show that *V. cholerae* MatP can delay segregation independently of tetramer
88 formation and any divisome interaction, and that the extent of the segregation delay is
89 determined by the number and local density of *matS* sites.

90 Results

91 Numerous *matS* sites flank both *dif1* and *dif2*

92 Based on the *E. coli matS* motif, 14 putative *matS* sites were identified in *TerII*[13]. This was in
93 apparent contradiction with the early separation and migration away from mid-cell of sister
94 *TerII* copies all the more as two *matS* sites are sufficient to bring a plasmid to mid-cell in *E.*
95 *coli*[9,10,15]. However, we noticed that a conserved amino acid motif differentiated the Vibrionales
96 and Enterobacterales MatP proteins[6]. It raised the possibility that *V. cholerae* MatP bound to
97 different DNA sites than *E. coli* MatP, which would be under-represented in *TerII*. To check
98 this possibility, we used ChIP-seq to explore the binding of *V. cholerae* MatP on ChrI and ChrII
99 *in vivo* (Methods). To this end, we introduced a FLAG tag allele of *matP* in place of the *matP*
100 gene (*matP3flag*). The choreography of segregation of sister *dif1* copies in cells harbouring
101 the *matP3flag* allele was identical to that of *matP*$^+$ cells, in contrast to Δ*matP* cells, indicating
102 that the allele was functional (Supplementary Fig. 1a).

103 The *matP3flag* ChIP-seq profile showed clearly distinguishable peaks (Fig. 1c). No peaks were
104 observed in the ChIP-seq profile obtained in a strain carrying a FLAG version of a C-terminal
105 truncation allele of *matP* that, based on the homology with *E. coli matP*, was expected to
106 prevent DNA binding by abolishing dimer formation (Supplementary Fig. 1b). These results
107 indicated that the peaks of the *matP3flag* ChIP-seq profile corresponded to MatP-binding sites
108 and that the C-terminal truncation allele of *V. cholerae matP* prevented the formation of MatP
109 dimers, i. e. it was a *matP* Δ*dimer* allele.
110 We identified 43 and 35 *matS* sites on ChrI and ChrII, respectively (Supplementary Data 1,
111 Supplementary Fig. 1c). Their consensus sequence was similar to the *E. coli matS* motif
112 (Supplementary Fig. 1d). No significant difference was observed in the sequence logos of the
113 ChrI and ChrII *matS* sites (Fig. 1c). We detected 66 additional putative *matS* sites in the *V.*
114 *cholerae* genome based on the *V. cholerae matS* consensus (Supplementary Data 2). No
115 enrichment was observed at the location of these sites, suggesting that they were not
116 functional (Supplementary Fig. 2).
117 Most of the *V. cholerae matS* sites were located in the terminal proximal part of the
118 chromosomes (Fig. 1c, Supplementary Data 1). The only notable exception was a site located
119 in the immediate vicinity of *ori2*. We previously noticed that *TerI* harboured a very strong SlmA
120 binding site (SBS) and a binding site for ParAB2 (*parS2*) separated by only 68 bp[4,23].
121 Therefore, we suspect that the presence of a *matS* site near *ori2* was caused by a translocation
122 event between this region and *TerI*.
123 The relative height of the ChIP-seq peaks tended to be higher near *dif1* and *dif2* (Fig. 1c). This
124 was not explained by any *matS* sequence specificity (Fig. 1d), but correlated with the local
125 density of *matS* sites (Fig. 1e). As the density of *matS* sites increases in the vicinity of *dif1* and
126 *dif2*, the cumulative binding of MatP was the highest at *dif1* and *dif2* (Fig. 1f).
127 **MatP structures *TerI* and *TerII* into macrodomains**
128 The *Ter* MD of the *E. coli* chromosome was defined as the longest stretch of DNA where *matS*
129 sites are separated by less than 100 kbp[13]. Based on the same criteria, 40 out of the 43 ChrI
130 *matS* sites defined a 659 kbp MD in the *TerI* zone, and 34 out of the 35 ChrII *matS* sites defined

131 a 546 kbp MD in the *TerII* zone (Fig. 1c, Supplementary Data 1). The mean density of *matS*
132 sites within these zones (~6 sites per 100 kbp) was twice higher than the mean density of *matS*
133 sites in the *E. coli Ter* MD (~3 sites per 100 kbp[13]). To check that MatP structured *TerI* and
134 *TerII* into MDs, we applied 3C coupled with deep sequencing (3C-seq) to exponentially growing
135 *matP*$^+$ and Δ*matP* N16961 cells. The contact map of WT cells showed a single strong diagonal
136 resulting from the enrichment of contacts between adjacent loci of each chromosome
137 (Supplementary Fig. 3a)[24]. The width of the diagonal was smaller in the *TerI* and *TerII* zones
138 than in the rest of the genome, reflecting a reduction of long-range *cis* contacts (Supplementary
139 Fig. 3a)[24]. Long-range *cis* contacts were recovered in Δ*matP* cells (Fig. 2, Supplementary Fig.
140 3b). In addition, the deletion of *matP* increased contacts between *ori2* and *TerII*, suggesting
141 that ChrII had entirely lost its structural conformation (Fig. 2).

142 **Deletion of *matP* leads to erratic positioning of *TerI* and *TerII***

143 We monitored the position of 12 loci in fluorescence snapshot microscopy images (Methods).
144 They included a locus at 53 kbp from *ori1* (OI), a locus at 24 kbp from *ori2* (OII), a locus right
145 next to *dif1* (DI) and a locus at 10 kbp from *dif2* (DII), 4 loci within the *TerI* MD (L5I, L6I, R6I
146 and R5I), 2 loci on the right replication arm of ChrI (R2I and R4I), and one locus on each of
147 the two replication arms of ChrII (L2II and R3II) (Fig. 1b).

148 Demographs (Methods) showed that the deletion of *matP* altered the positioning and
149 choreography of segregation of all loci but OI and OII (Supplementary Fig. 4). To quantify the
150 effect of the deletion of *matP*, we analysed the cellular position of spots before their duplication
151 in cells at an early stage of the cell cycle and after their duplication in cells at a late stage of
152 the cell cycle, hereafter referred to as young and old cells (Methods). In young *matP*$^+$ cells,
153 *TerI* loci were all constrained at a median distance of ~15% of the cell length from the new pole
154 (Fig. 3a). The median distance increased to ~33% of the cell length in Δ*matP* cells (Fig. 3a).
155 In contrast, *TerII* loci were positioned at a median distance of ~30% of the cell length in both
156 *matP*$^+$ and Δ*matP* cells (Fig. 3a). However, the deletion of *matP* increased the interquartile
157 distribution of the distance of *TerII* loci from the new pole to ~27% of the cell length, as it did

158 for *TerI* loci (Fig. 3a). The same trend was observed for the position of sister spots of old cells
159 (Supplementary Fig. 5a).
160 To further highlight the effect of MatP on the cellular arrangement of ChrI and ChrII, we plotted
161 the median distance between sister spots in old cells (Fig. 3b). In *matP*$^+$ cells, DI, L5I, L6I, R6I,
162 R5I and R4I sister spots were closer than expected from a linear increase as a function of their
163 genomic distance from OI (Fig. 3b). In particular, the median distance between DI, L6I, and
164 R6I sister spots was lower than ~4% of the cell length (Fig. 3b). Deletion of *matP* increased
165 the median distance between sister spots of *TerI* loci to ~27% of the cell length (Fig. 3b). In
166 contrast, DII, L2II and R3II sister spots were at a median distance from each other of ~15% of
167 the cell length in both *matP*$^+$ and Δ*matP* cells (Fig. 3b). However, the deletion of *matP*
168 increased the interquartile distribution of *TerII* sister spot distances to ~25% of the cell length,
169 as it did for *TerI* loci (Fig. 3b). The deletion of *matP* also altered R4I and R2I sister spot
170 distances, notably by increasing their interquartile distribution (Fig. 3b).
171 Taken together, these results showed that MatP constrained the central part of the *TerI* MD to
172 the new pole in young cells and to mid-cell in old cells, which affected a large 1 Mbp zone
173 extending outside of the *TerI* MD (Fig. 3a and 3b). In contrast, MatP was not able to tether
174 *TerII* loci at the new pole in young cells and at mid-cell in old cells. However, our results
175 suggested that the positioning of all ChrI and ChrII loci but OI and OII was more erratic in
176 Δ*matP* cells.
177 **MatP is involved in *dif1*- and *dif2*-cohesion at the onset of division**
178 In *matP*$^+$ cells, the spot duplication frequency of ChrI loci did not follow their timing of
179 replication[7]: it was similar at OI and R2I, but dropped abruptly inside the *TerI* MD (Fig. 3c).
180 Likewise, the spot duplication frequency of DII was lower than expected from its replication
181 timing (Fig. 3c). Deletion of *matP* suppressed the separation delay of *TerI* loci and that of DII,
182 with the spot duplication frequency now reflecting their timing of replication (Fig. 3c). In
183 addition, the duplication increase was much larger in the immediate vicinity of DI and DII than
184 at loci at the border of the *TerI* and *TerII* MDs (grey bars in Fig. 3c). These observations
185 suggested that MatP increased cohesion.

186 To further investigate the role of MatP in sister chromatid cohesion, we monitored the
187 frequency of sister chromatid contacts behind replication forks (f_{rep}) and at the time of cell
188 division (f_{div}) with a high-resolution whole-genome method, Hi-SC2 (Methods).
189 In *matP*$^+$ strains, f_{rep} was higher in the *TerI* and *TerII* MDs than in the rest of the genome and
190 was maximal at *dif1* and *dif2* (Fig. 3d). Deletion of *matP* did not modify f_{rep} along ChrI except
191 in the *TerI* MD where ~40% of the sister chromatid contacts were lost (Fig. 3d, Supplementary
192 Fig. 5b). It increased f_{rep} in the replication arms of ChrII except in a 150 kbp zone within the
193 *TerII* MD where ~40% of the sister chromatid contacts were lost (Fig. 3d, Supplementary Fig.
194 5b).
195 In *matP*$^+$ cells, f_{div} was null at all genomic positions except in the immediate vicinity of *dif1* and
196 *dif2* (Fig. 3e, Supplementary Fig. 5c). Note that a large *dif1* cassette, which allows intra-
197 molecular recombination, was excised at a frequency greater than 50% in a third of ChrI and
198 half of ChrII (Supplementary Fig. 5d), excluding the idea that Xer recombination could only
199 occur in the vicinity of *dif1* and *dif2* because of FtsK is directed towards them by orienting polar
200 sequences [8,25–28]. In Δ*matP* cells, ~70% and 60% of *TerI* and *TerII* sister chromatid contacts
201 at cell division were lost, respectively (Fig. 3e, Supplementary Fig. 5c).
202 Taken together, these results indicated that MatP was involved in the post-replicative cohesion
203 of loci within the *TerI* and *TerII* MDs and played a major role in the persistence of cohesion
204 until the initiation of cell division in the immediate vicinity of *dif1* and *dif2*.
205 **MatP extends cohesion between consecutive MatP domains**
206 To gain further insight into the role of MatP in the arrangement and segregation of
207 chromosomes, we analysed its action in the synthetic monochromosomal MCH1 strain (Fig.
208 4a)[29]. Previous work showed that replication of the MCH1 chromosome starts at *ori1* and ends
209 in *TerII*[4], and that chromosome dimers are efficiently resolved by Xer recombination at *dif2*[29].
210 ChIP-seq showed that there are 3 MatP domains in the MCH1 chromosome, the *TerII* MD and
211 the Right and Left part of the *TerI* MD (Fig. 4b, Supplementary Fig. 6a, Supplementary Data
212 4). The most highly enriched sequences were located at the centre of the *TerII* MD (Fig. 4b,

213 note that the highly enriched *matS* site located near *ori2* in N16961 is absent from the MCH1
214 chromosome). Sequences in the Right *TerI* MD were as enriched as sequences in the *TerII*
215 MD, but the enrichment of sequences in the Left *TerI* MD was very poor (Fig. 4b,
216 Supplementary Fig. 6a).
217 We monitored the position of 11 loci in fluorescence snapshot microscopy images, including
218 the OI, OII and DII loci, 5 loci on the right replication arm (R1I, R3I, R5I, OII and L1II) and 4
219 loci on the left replication arm (R3II, R1II, L6I and L5I) of the chromosome (Fig. 4a).
220 Demographs showed that MatP was involved in the choreography of segregation of L6I, R3II,
221 DII, L1II and OII (Supplementary Fig. 6b and 6c). In young *matP*$^+$ MCH1 cells, the distance
222 between the spot of each labelled locus and the new pole increased almost linearly as a
223 function of their genomic distance from DII (Fig. 4c). DII was closer to the new pole than it was
224 in young N16961 cells (Fig. 4c). The same trend was observed in old cells for the distance of
225 sister spots from the centre of the cell (Supplementary Fig. 6d) and the distance between sister
226 spots (Fig. 4d). Loci comprised between OII and L6I were further away from the new pole in
227 young MCH1 Δ*matP* cells than in *matP*$^+$ cells (Fig. 4c). DII was at the same distance from the
228 new pole in young MCH1 Δ*matP* cells than it was in N16961 Δ*matP* cells (Fig. 4d). The same
229 trend was observed for the distance of sister spots from the centre of the cell (Supplementary
230 Fig. 6d) and the distance between sister spots (Fig. 4d). These results suggested that MatP
231 played a significant role on the arrangement of the MCH1 chromosome.
232 Strikingly, the spot duplication frequency was low in the vicinity of DII but also at OII, L6I, R1II,
233 R3II, R5I and L5I (Fig. 4e). Correspondingly, f_{rep} was high within *TerII*, the right half of *TerI*,
234 and all the intermediate positions between these two zones (Fig. 4f, Supplementary Fig. 6e).
235 In addition, f_{div} was highly elevated in the 800 kbp zone comprised between DII and R5I (Fig.
236 4g, Supplementary Fig. 6f). Deletion of *matP* only slightly increased f_{rep} in the regions
237 corresponding to ChrI (Fig. 4f, Supplementary Fig. 6e). However, it led to a ~25% reduction in
238 sister chromatid contacts behind replication forks in the 150 kbp zone surrounding *dif2* and
239 resulted in the loss of ~80% of the sister chromatid contacts in the DII-R5I region at the time
240 of cell division (Fig. 4g, Supplementary Fig. 6f). These results indicated that MatP was able to

241 maintain together sister copies of loci between the MCH1 *TerII* MD and the Right *TerI* MD, but
242 failed to maintain together sister copies of loci in the Left *TerI* MD.

243 **MatP-mediated cohesion depends on the number and local density of *matS* sites**

244 The number and density of *matS* sites of the Left *TerI* MD of the MCH1 chromosome is lower
245 than that of the Right *TerI* MD, which suggested that a threshold had to be reached for the
246 effect of MatP on cohesion to be visible (Fig. 4b). To test this hypothesis, we displaced two
247 *matS* sites adjacent to *dif1* in ChrI next *dif2* in ChrII (Fig. 5a, JVV024). It decreased the density
248 of *matS* sites in the *TerI* MD from 6.1 to 5.8 sites per 100 kbp and increased the density of
249 *matS* sites in the *TerII* MD from 6.2 to 6.6 sites per 100 kbp (Supplementary Data 5), which
250 mitigated the difference in the enrichment of MatP at DI and DII (Fig. 5b). Shifting the two *matS*
251 sites increased f_{div} at the DII locus (Fig. 5c, Supplementary Fig. 7a). Demographs showed no
252 obvious difference between the choreography of segregation of DI and DII in JVV024 and
253 N16961 (Supplementary Fig. 7b). However, the distance separating DI sister copies was
254 slightly but significantly higher in JVV024 cells than in N16961 cells (Fig. 5d, Supplementary
255 Table 1). In addition, the relative timing of appearance of two DI spots loci was now similar to
256 that of DII spots (Supplementary Fig. 7c). Correspondingly, the proportion of cells showing a
257 single DII spot and two DI spots was significantly higher than that of cells showing two DII
258 spots and a single DI spot in JVV024 compared to N16961 (Fig. 5e, Supplementary Table 2).
259 These results suggested that MatP influenced cohesion at the time of cell division at positions
260 where it was highly enriched, namely *dif1* and *dif2* in N16961 (Fig. 1f), and *dif2* and the junction
261 of ChrII DNA with the Right *TerI* MD in MCH1 (Supplementary Fig. 6a). To test this hypothesis,
262 we constructed a strain in which the right part of the *TerI* MD was inverted, EPV487 (Fig. 5f).
263 The inversion created a cleft in the MatP ChIP-seq profile at *dif1* (Fig. 5g, Supplementary Data
264 6). The position with the highest MatP enrichment was now at the junction of the inverted
265 fragment and the right replication arm (Fig. 5g). The f_{div} profile followed the local enrichment
266 of MatP (Fig. 5h, Supplementary Fig. 7d). As with N16961 and MCH1, the elevated f_{div} was
267 mainly associated with MatP (Supplementary Fig. 7e). Demographs showed no obvious
268 difference between the choreography of segregation of DI and DII in EPV487 and N16961

269 (Supplementary Fig. 7b). However, the inversion significantly affected the distance between
270 DI and DII sister copies (Fig. 5d, Supplementary Table 1). In addition, the relative timing of
271 appearance of two DI spots was now earlier than that of DII spots (Supplementary Fig. 7c).
272 Correspondingly, the proportion of cells showing two DI spots and a single DII spot was
273 significantly higher than that of cells showing a single DI spot and two DII spots in EPV487
274 cells compared to N16961 cells, reflecting the decrease in cohesiveness of the DI sister copies
275 (Fig. 5e, Supplementary Table 2).

276 **MatP acts independently of cell division**

277 A plasmid with two *matS* sites accumulates at mid-cell in a MatP dependent manner in *E.*
278 *coli*[15]. The localisation pattern of the plasmid was shown to be due to the formation of a
279 proteinaceous bridge between the tetramerization domain of MatP, ZapB, ZapA and FtsZ [15,18].
280 In *V. cholerae*, DI localised at mid-cell at the time of cell division, consistent with the idea that
281 MatP coordinated chromosome segregation and cell division by tethering MatP domains to the
282 divisome (Fig. 3a and Supplementary Fig. 5a). However, DII did not localise at mid-cell at the
283 time of division (Fig. 3a and Supplementary Fig. 5a) even though it is flanked by 34 *matS* sites
284 (Fig. 1c). Therefore, we decided to explore the role of the tetramerization domain of MatP,
285 ZapB and ZapA in the positioning of DI and DII.

286 To this end, we constructed an allele of *matP* truncated from the extreme C-terminus, which
287 based on the homology with *E. coli matP* should prevent the formation of MatP tetramers,
288 *matP* Δ*tetra*. MatP Δtetra had the same binding profile as WT MatP (Supplementary Fig. 8a).
289 We then compared the cellular position of DI and DII in parallel with that of OI in WT, Δ*matP*,
290 *matP* Δ*dimer*, *matP* Δ*tetra*, Δ*zapA* and Δ*zapB* N16961 strains in snapshot images.
291 Demographs suggested that the choreography of segregation of DI and DII in *matP* Δ*tetra*,
292 Δ*zapA* and Δ*zapB* cells was similar to that of WT cells, in contrast to that of Δ*matP* and *matP*
293 Δ*dimer* cells (Supplementary Fig. 8b). To quantify the effect of the *matP* Δ*tetra*, Δ*zapA* and
294 Δ*zapB* mutations on the cellular position of DI and DII, we analysed the distance separating
295 sister DI copies and sister DII copies. Whereas the distance between sister DI copies was as
296 elevated as that of sister DII copies in Δ*matP* and *matP* Δ*dimer* cells, it was significantly lower

297 than that of DII in the *matP* Δ*tetra*, Δ*zapA* and Δ*zapB* mutants (Fig. 6a, Supplementary Table
298 3). However, we noticed that the distance between sister DI copies was slightly – yet
299 significantly - elevated in the *matP* Δ*tetra*, Δ*zapA* and Δ*zapB* (Fig. 6a, Supplementary Table
300 3). Hence, we decided to follow the choreography of segregation of DI by time-lapse video
301 microscopy. Results recapitulated those of the demographs. In the presence of MatP, DI
302 localised at the new pole of newborn cells and migrated to mid-cell at the very end of the cell
303 cycle, with sister DI copies remaining associated until the very end of the cell cycle (Fig. 6b).
304 In Δ*matP* cells, DI was randomly distributed between the new pole and mid-cell at birth and
305 the ¼-¾ part of the cell at the end of the cell cycle (Fig. 6b). Inspection of individual traces
306 further showed that sister DI copies separated prior to cell division with a distance of over a
307 quarter of the cell length (Supplementary Fig. 9b). Cells carrying the *matP* Δ*dimer* allele had
308 the same phenotype as Δ*matP* cells (Fig. 6b). In *matP* Δ*tetra*, Δ*zapA* and Δ*zapB* cells, the
309 fluorescence signal was less marked at the new pole of new born cells than in WT cells (Fig.
310 6b). Nevertheless, the choreography of segregation remained similar to that of WT cells (Fig.
311 6b).
312 To rule out the possibility that another cell division protein was involved in the action of MatP
313 on the positioning of *TerI* and *TerII* at mid-cell, we compared the choreography of DI
314 segregation in *matP*$^{+}$ and Δ*matP* cells carrying a thermosensitive allele of *ftsZ*, *ftsZ84*^{ts}. Growth
315 of *ftsZ84*^{ts} strains at the non-permissive temperature (42°C) prevents the formation of the FtsZ
316 ring, which leads to the dispersal of the other cell division proteins in the cytoplasm of the cell
317 and filamentation[5]. The binding profile of MatP on the genome of *ftsZ84*^{ts} cells grown at 42°C
318 was identical to the binding profile of MatP on the genome of WT N16961 cells and *ftsZ84*^{ts}
319 cells grown at the permissive temperature (30°C) (Supplementary Fig. 9c). However, DI copies
320 separated from each other at a much later stage in the *ftsZ84*^{ts} strain grown at 42°C than in its
321 Δ*matP* derivative (Fig. 6c, Supplementary Movies 1 and 2).
322 Taken together, these results showed that MatP was able to keep sister *dif1* sites together at
323 mid-cell independently of tetramer formation and divisome anchoring.

324 ## Discussion

325 ***TerI* and *TerII* both contain a high density of *matS* sites**

326 The *V. cholerae matS* sites we identified are similar to the *E. coli matS* sites, but more diverse
327 (Fig 1, Supplementary Fig. 1), which explains why only 34 and 14 *matS* sites were predicted
328 on ChrI and ChrII based on the *E. coli matS* motif[13]. The relative height of the ChIP-seq profile
329 at the location of the *matS* sites was similar in the different ChIP-seq experiments we
330 performed in the course of this study (Fig. 1, 4, 5, Supplementary Fig. 8 and 9). The ChIP-seq
331 profile tended to be higher at the centre of the *TerI* and *TerII* MDs. This was not linked to any
332 bias in the identity score of the sites at the centre of the domains (Fig. 1, Supplementary Data
333 1). The MCH1 and EPV487 data further ruled out that it was linked to the timing of replication
334 and the action of FtsK (Fig. 4 and 5). Instead, it seemed linked to the increase in the local
335 density of *matS* sites at the centre of the *TerI* and *TerII* MDs (Fig. 1). The presence of a *matS*
336 site in a phage satellite that is integrated in two copies next to *dif1* (TLCΦ), in several cassettes
337 of the super-integron, which is located next to *dif2*, and in the coding sequence of genes,
338 suggests that there is a selection pressure to maintain the number and local density of *matS*
339 sites. We detected additional *matS* binding sites on the genome of *V. cholerae* that were not
340 enriched in the ChIP-seq experiments despite a good identity score (Supplementary Fig. 2). It
341 suggests that cellular factors, such as other DNA binding proteins and ongoing transcription,
342 probably hinder MatP binding at these positions.

343 ***TerI* and *TerII* cohesion and positioning are functionally distinct from MD formation**

344 Our results suggest that MatP plays the same two roles *in V. cholerae* as it does in *E. coli*. On
345 one hand, it structures *TerI* and *TerII* into macrodomains, which are isolated from the rest of
346 the genome (Fig. 2). On the other hand, it is involved in the cohesion period of *TerI* and *TerII*
347 sister copies behind replication forks, the persistence of cohesion until the initiation of cell
348 division in the vicinity of *dif1* and *dif2*, and the positioning of *TerI* and *TerII* loci towards the new
349 pole in young cells and to mid-cell in old cells (Fig. 3).

350 However, a clear distinction could be made on the mode of action of MatP in MD formation
351 and segregation. The reduction of long-range *cis* contacts was as important at the border of

352 the *TerI* and *TerII* MDs as in their central part (Fig. 2). This is consistent with *E. coli* studies
353 that suggested that a few *matS* sites were sufficient for MatP to exclude and/or inactivate a
354 DNA condensin, MukBEF, that favours long-range *cis* contacts by extruding ~800 kbp
355 intrachromosomal loops[13,14,30–33]. Future work will need to investigate the interplay between
356 MatP and MukBEF in the structuration of the chromosomes in *V. cholerae*. In contrast,
357 cohesion behind replication forks was lower at the border of the *TerI* and *TerII* MDs than in
358 their central part (Fig. 3). In addition, cohesion only persisted until the initiation of cell division
359 at the very centre of the *TerI* and *TerII* MDs (Fig. 3).

360 **Another factor than MatP is involved in the cohesion of *TerI* and *TerII* loci**

361 The deletion of *matP* only partially alleviated the high post-replicative cohesion of *TerI* and
362 *TerII* loci, suggesting the implication of another factor than MatP in the phenomenon (Fig. 3
363 and 4). In contrast, the deletion of *matP* almost entirely suppressed the persistence of cohesion
364 until the initiation of cell division in the immediate vicinity of *dif1* and *dif2* (Fig. 3 and 4).

365 **Cohesion and positioning depend on the number and local density of *matS* sites**

366 Loci at the centre of the *TerI* MD were the closest to the new pole in young cells and sister
367 copies of these loci were the closest to each other and to mid-cell in old cells, in agreement
368 with the persistence of cohesion (Fig. 3). This was not true for *TerII* loci, for which the deletion
369 of *matP* only increased the range of the positions that they could occupy, and for which the
370 persistence of cohesion until cell division was very limited (Fig. 3). We suspected that
371 differences in the cohesion and cellular positioning of *TerI* and *TerII* loci were at least in part
372 due to differences in the number and density of *matS* they contained. This hypothesis was
373 corroborated with results in three synthetic strains in which the chromosomal distribution of the
374 *matS* sites was altered, MCH1, JVV024 and EPV487: the Right *TerI* MD of MCH1, which
375 harbours 26 *matS* sites, was highly cohesive whereas the Left *TerI* MD of MCH1, which
376 harbours 12 *matS* sites, was not (Fig. 4); differences in the cohesion of sister copies of *dif1*
377 and *dif2* loci were alleviated in JVV024, in which the number of *matS* sites in the *TerI* MD was
378 reduced from 40 to 38 and that of the *TerII* MD was increased from 34 to 36 (Fig. 5); the

379 frequency of sister chromatid contacts at the time of cell division followed the density of *matS*
380 sites in MCH1 and EPV487 (Fig. 4 and 5).

381 **MatP-mediated positioning is independent of cell division and tetramer formation**

382 The precise mid-cell positioning of *dif1* at the end of the replication cycle and the proximity of
383 sister *dif1* copies after their separation were not altered in Δ*zapA* and Δ*zapB* cells (Fig. 6).
384 Likewise, recent high throughput time-lapse observations showed that mid-cell migration of the
385 *Ter* was barely modified in Δ*zapB E. coli* cells[17]. In the present study, we further show that
386 MatP delays the separation of sister *dif1* copies in *ftsZ84*^{ts} cells grown at the non-permissive
387 temperature, thereby demonstrating that mid-cell positioning is independent of any anchoring
388 to a divisome component (Fig. 6).

389 MatP tetramers have also been proposed to mediate cohesion by linking *matS* sites together
390 and/or to non-specific DNA in *E. coli*[12,16,17]. In contrast, we found that deletion of the
391 tetramerization domain of MatP barely altered the mid-cell positioning of *dif1* and the distance
392 of separation of sister *dif1* copies, thereby demonstrating that tetramer formation plays little or
393 no role in the cohesion and mid-cell positioning of sister DNA copies in *V. cholerae* (Fig. 6).

394 Instead, our results are consistent with a role for MatP in the regulation of decatenation. Due
395 to the helical nature of double stranded DNA, (+) supercoils accumulate ahead of replication
396 forks. The torsional stress is thought to cause the replication machinery to swivel around itself,
397 generating right-handed interlinks that must be removed by topoisomerase IV (Topo IV).
398 MukBEF has been shown to trail behind replication forks and recruit Topo IV in *E. coli*[13,34,35].
399 However, cohesion at the time of cell division was higher in the central part of the *TerI* and
400 *TerII* MDs than at their borders (Fig. 3), in contrast to the restriction of long-range *cis* contacts
401 (Fig. 2), suggesting that MatP could slow decatenation independently of its effect on MukBEF.
402 The decrease in cohesion between the Right *TerI* MD and the *TerII* MD domain of MCH1 (Fig.
403 4) and at *dif1* in the *TerI* MD of EPV487 (Fig. 5) further suggests that the prolonged period of
404 precatenane persistence in the central part of the *TerI* and *TerII* MDs is not related to their
405 timing of replication nor to the oriented translocation of FtsK[36,37], but to the high density of *matS*
406 sites they contained. Finally, the earlier separation and greater distance between sister copies

407 of *dif2* than sister copies of *dif1* suggest that decatenation is faster in *TerII* than in *TerI* due to
408 a lower number and density of *matS* sites (Fig. 3). The short length of ChrII could also reduce
409 the chances of leaving unresolved catenation links behind replication forks and lead to a tug-
410 of-war between the ParAB2/*parS2* and MatP/*matS* systems, which could help separate sister
411 copies of *TerII*. Consistent with this view, sister *TerII* copies in MCH1 separated later, were
412 positioned closer to each other in old cells and to the cell pole in young cells than sister *TerII*
413 copies in N16961 (Fig. 4).
414 It is likely that MatP-mediated inhibition of decatenation is also responsible for the initial
415 positioning of sister copies of the *Ter* at mid-cell in *E. coli*. Consistent with this view, it was
416 recently reported that sister *Ter* copies separated but remained in close proximity to mid-cell
417 in Δ*zapA* and Δ*zapB* mutants[17]. Decatenation could be more effective in *E. coli* than in *V.*
418 *cholerae* because of the lower number and density of *matS* sites in *Ter* than in *TerI* and *TerII*,
419 which could further explain the importance of the MatP-ZapB-ZapA connection for the
420 maintenance of sister *Ter* copies at mid-cell until the final stages of cell division.
421 Future work will need to develop a methodology to directly monitor the catenation links that
422 remain to be removed at the end of the replication cycle in *E. coli* and *V. cholerae*.
423 **ChrII behaves as a *bona fide* bacterial chromosome from a functional point of view**
424 ChrI is derived from the chromosome of the monochromosomal ancestor of the Vibrionales
425 and Enterobacterales, whereas ChrII is derived from a megaplasmid[38]. From a genomic point
426 of view, ChrII is considered as a 'chromosome-plasmid', or chromid, because it carries
427 essential core genes, has a nucleotide composition close to that of ChrI, but possesses
428 plasmid-type replication and partition systems[39]. However, we previously showed that ChrII
429 participates to the regulation of the cell cycle because its origin proximal part is enriched in
430 SlmA-binding sites[4]. Our ChiP-seq, 3C-seq, fluorescence microscopy and Hi-SC2 results
431 further demonstrate that MatP structures *TerII* into a macrodomain, coordinates its migration
432 with that of *TerI* and ensures its positioning close to mid-cell at the time of cell division, which
433 is essential for the control of cell division by SlmA-mediated nucleoid occlusion (Fig. 1, 2, 5).

434 In this regard, ChrII is organised and behaves as a *bona fide* bacterial chromosome. It will be
435 interesting to check whether such a functional definition applies to other chromids.

436 Methods

437 **Strains, plasmids and oligonucleotides**

438 Bacterial strains, plasmids and oligonucleotides used in this study are listed in Supplementary
439 Table 4. All strains are derivatives of an El Tor N16961 strain that was rendered competent by
440 the insertion of *hapR* by specific transposition. They were constructed by natural
441 transformation or conjugation with integration/excision plasmids. Strains construction is
442 described in detail in Supplementary Information. Engineered strains were confirmed by PCR.
443 Chromosomal loci were visualised by inserting a $parS^{pMT1}$ motif specifically detected by YGFP-
444 $ParB^{pMT1}$ or a *lacO* array specifically detected by LacI-RFPT or LacI-mCherry[40,41]. The list of
445 the strains that were used in each figure panel are detailed in Supplementary Information.
446

447 **ChIP-seq**

448 ~10^9 cells from overnight cultures harbouring a functional *matP3flag* allele at the *matP* native
449 locus were diluted into 100 mL of fresh media and were grown until exponential phase (OD_{600}
450 0.2). Cells were crosslinked for 30' with formaldehyde 37% up to a final concentration of 1%.
451 Crosslinking reactions were quenched for 15' with Glycine 2.5 M up to a final concentration of
452 250 mM. Samples were centrifuged, washed with TBS (Tris-HCl pH 4.7 50 mM, NaCl 1M) and
453 harvested by centrifugation. After, cells were lysed for 30' at 37°C with 500 µL of lysis buffer I
454 (sucrose 20%, Tris-HCl pH 8 10 mM, NaCl 50 mM, EDTA 10 mM and Lysozyme 1 mg/mL
455 (w/v)). Then, 500 µL of lysis buffer II (Tris-HCl pH 4.7 50 mM, NaCl 150 mM, EDTA 1mM,
456 Triton X100 1%, Roche Antiprotease Cocktail) was added and samples were sonicated for 30'
457 (Covaris, Duty cycle 5, Intensity 4, Cycle/burst 200). After sonication, samples were
458 centrifuged at 17949 g for 30' at 4°C. Supernatants were collected into a fresh tube, 50 µL
459 were separated to use as control (Input). For immunoprecipitation (IP), an Anti-FLAG M2
460 affinity gel (Sigma) was added to the cell extracts and the volume was adjusted up to 1 mL in

461 lysis buffer II. After an overnight incubation at 4°C on a rotating wheel, samples were
462 centrifuged at 3824 g for 30 seconds at 4°C. Pellets were washed twice with TBS mixed with
463 Tween 20 0.05% and three times with TBS. A 3xFLAG elution solution was prepared in buffer
464 (Tris-HCl pH 4.7 500 mM, NaCl 1M) at a concentration of 25 µg/µL and diluted in TBS to a
465 final concentration of 150 ng/µL. 2.5 volumes of elution solution were added per volume of IP
466 sample and Input. Samples were incubated for 30' at 4°C on a rotating wheel. Then, samples
467 were eluted twice by centrifugation at 3824 g for 30 seconds at 4°C. RNase A was added to a
468 final concentration of 1 µg/mL and samples were incubated for 1 hour at 37°C. Finally, samples
469 were de-crosslinked by the addition of 5 µL of proteinase K (20 mg/mL) and overnight
470 incubation at 65°C. The genomic DNA from the Input and the IP sample was extracted using
471 a Qiagen PCR Purification Kit and Qiagen MinElute PCR Purification Kit, respectively. Illumina
472 libraries were prepared using DNA SMART™ ChIP-Seq Kit (TAKARA) following manufacture's
473 protocol. Purified libraries were subjected to sequencing on a NextSeq 500 (Illumina). After
474 sequencing, barcodes and adapters were removed using Cutadapt [42] and files with total reads
475 were created. Finally, the BWA software was used for the alignment of reads on genomes[43]
476 and the data was stored in the SAM format [44].
477 We used custom MatLab functions for plotting and analysis purposes (see Code availability).
478 In brief, Input and ChIP read numbers were smoothed with a 101 bp sliding window, and
479 divided by the total number of reads. Positions where the Input reads were twice higher or
480 twice lower than the median of the 200001 Input reads surrounding them were replaced by
481 NaN (Not a Number). We then computed the ratio of the ChIP read over the Input read at each
482 position of each chromosome. We retrieved the 100 bp sequence surrounding genomic
483 locations with a height 3 times higher than the median of the ChIP-seq profile. MEME analysis
484 of the sequences using default parameters revealed the presence of a 13 bp DNA motif. We
485 set the length of the motif to be exactly 13 bp in the MEME parameters to determine the
486 position-specific probability matrix of the motif, and used it to scan the *V. cholerae* genome
487 with MCAST. All of the motifs identified with MEME were retrieved in the MCAST motif table,
488 which permitted to assign a quality score to their sequence (Supplementary Data 1). MCAST

489 permitted to detect 11 additional sites at the positions of which the ChIP-seq profile was
490 elevated (Supplementary Data 1, Supplementary Fig. 1d) and 66 sites with a quality score
491 higher than the smallest quality score of Supplementary Data 1 sites at the positions of which
492 the ChIP-seq profile was not elevated (Supplementary Data 2, Supplementary Fig. 2).

493 **Fluorescence microscopy**

494 Cells were grown in M9 minimal medium supplemented with 0.2% fructose and 1 µg/mL
495 thiamine. In this medium, cells perform a single replication/segregation cycle per division.
496 Thus, each labelled locus gives rise to one or two spots, depending on whether it has been
497 replicated and sister copies have separated or not [9]. Cells were grown to exponential phase in
498 liquid and spread on a 1% (w/v) agar pad (ultrapure agarose, Invitrogen). Snapshot images
499 were acquired using a Prime BSI camera (Roper) attached to DM6000-B (Leica) microscope
500 (Excitation source: HPX; Cubes with pass band 480/30 and 560/40 nm excitation filters, 505
501 and 600 nm dichroic mirrors, and pass band 535/40 and 635/60 nm emission filters). For time-
502 lapse analyses, the slides were incubated at 30°C (and 42°C for *ftsZ84*^{ts} strains) and images
503 were acquired every 3' or 4' using an Evolve 512 EMCCD camera (Roper Scientific) attached
504 to an Axio Observer (Zeiss) with a CXUI spinning disk (Yokogawa) equipped with a triple band
505 dichroic filter (Di01-405/488/561) and a pass band FF03-525/50-25 and long pass BLP01-
506 561R-25 on a filter wheel. 488 nm and 561 nm 150 mW diode lasers (at 20% of their maximal
507 delivery) were used for excitation. The list of the strains that were used in each figure panel
508 are detailed in supplementary

509 **Snapshot image analysis**

510 Cell outlines were generated using MicrobeTracker and spots were detected with SpotFinder[45].
511 Cell outlines and spot locations were manually curated. We used custom MatLab functions to
512 analyse the cell Lists (See Code availability). In brief, cells were oriented on the basis that OI
513 is located at the old pole of newborn cells whereas DI and DII are located at the new pole of
514 newborn cells and that during the replication/segregation cycle, one of the two sister OI copies
515 remains at the old pole and the other one migrates to the opposite pole, whereas sister DI and

516 DII copies migrate to mid-cell and split just before cell division[9]. Demographic representations
517 (demographs) were plotted to provide an indirect view of the cell cycle choreography of loci.
518 The x- and y-axes of demographs correspond to the ranking number of cells when ordered
519 according to their length and the longitudinal coordinate of the cells, respectively. Taking into
520 account that cell length increases exponentially during the cell cycle, the ranking number can
521 be used to estimate the advancement of the cell cycle [5]. The numbers of cells analysed for
522 each demograph is indicated in Supplementary Data 3.
523 The ranking number was used to determine the length of cells that had reached 33% and 75%
524 of the cell cycle for each of the analysed strains. The young cells of each tagged locus were
525 defined as the cells with a length smaller than the 33% cell cycle length in which the
526 fluorescence label of the focus gave rise to a single spot, and the old cells as those with a
527 length longer than the 75% cell cycle length in which the fluorescence label of the focus gave
528 rise to two spots. The number of young and old cells for each locus of the analysed strains is
529 indicated in Supplementary Data 3.
530 **Time-Lapse analysis**
531 To follow the positions of labelled loci in the course of the cell cycle, we performed time lapse
532 observations of cells growing in microcolonies. Cell contours were detected and cell
533 genealogies were retraced with a MatLab script based on MicrobeTracker [4]. After the first
534 division event, the new pole and old pole of cells can be unambiguously attributed based on
535 the previous division event. We used a custom MatLab function to create heat map
536 representations of the position of labelled loci (See Code availability). In brief, the heat maps
537 were built using cells that were born and divided in the course of the time lapse observations,
538 i.e cells that had completed their cell cycle. The number of such cells is indicated in
539 Supplementary Fig. 9a for each strain. Note that, because of the time interval between time
540 points, the first image of the time lapse of these cells does not correspond to their exact timing
541 of birth and their last image does not correspond to the exact timing of its division. The single
542 traces were aligned using the first image following birth and the last image before division. Fluo
543 projections were then rescaled to accommodate for differences in the length of the cells in the

544 first image and last image of their cell cycle and in the time interval between the first image
545 and the last image of their cell cycle. The x-axis corresponds to the relative advancement of
546 the cell cycle from the first image after birth to the last image after birth.

547 **Hi-SC2**

548 Hi-SC2 uses paired-end sequencing to determine the status and position of site-specific
549 recombination cassettes that have been randomly-inserted by transposition[46]. The cassettes
550 are composed of two directly repeated recombination sites separated by a DNA segment that
551 is too short to allow their excision by intramolecular recombination. However, intermolecular
552 recombination events between sister copies of a cassette can lead to the formation of a copy
553 with a single recombination site. Therefore, the excision frequency of the cassette, f, can be
554 used as a proxy of the length of time during which sister copies remain in contact. The local
555 frequency of sister chromatid contacts behind replication forks can be monitored using
556 cassettes based on the Cre/*loxP* site-specific recombination system, whose activity is
557 independent of the cell cycle[47,48]. The local frequency of sister chromatid contacts at the onset
558 of constriction can be monitored using cassettes based on the XerCD/*dif1* site-specific
559 recombination system, whose activity depends on a direct contact with a cell division protein,
560 FtsK[8,10]. Hi-SC2 transposon libraries were prepared [49]. Briefly, transposons harbouring *loxP* or
561 *dif1* cassettes and a kanamycin resistance gene were introduced in strains conditionally
562 expressing Cre or XerC, respectively. Tight control of the recombinase production was
563 achieved by placing their genes under an arabinose promoter and an antisense β-
564 galactosidase promoter. After overnight growth on LB plates containing kanamycin and IPTG,
565 ~400.000 colonies were scraped, mixed in LB with IPTG and stored in aliquots at -80°C.
566 Aliquots of the transposon library were thawed on ice and $\sim 10^9$ cells were diluted into 100 mL
567 of media supplemented with IPTG. Cells were grown until exponential phase (OD_{600} 0.2). Then,
568 $\sim 10^9$ cells were centrifuged and transferred into 10 mL of fresh media without IPTG. After 30',
569 arabinose was added at a final concentration of 0.02%. $\sim 10^9$ cells were recovered and frozen
570 in liquid nitrogen after 5 hours of induction for *dif1* cassettes and 90' for *loxP* cassettes.
571 Genomic DNA was subjected to pair-end sequencing on a NextSeq 500 (Illumina) to determine

572 the position of the reporters and their recombination status. Sam files were generated using
573 Cutadapt and BWA[42–44]. The data were analysed with custom MatLab functions (see Code
574 availability).

575 **Generation of 3C libraries**

576 3C libraries were generated as described[24]. In brief, cultures were crosslinked with
577 formaldehyde (3%). Fixed cells were lysed with SDS (0.5%) in the presence of lysozyme (35
578 U/mL; Tebu Bio). Their genome was subjected to HpaII digestion and re-ligation. The DNA
579 was then purified and quantified on gel using QuantityOne software (BioRad). The resulting
580 3C library was sheared using a Covaris S220 instrument (Duty cycle 5, Intensity 5, cycles/burst
581 200, time 60 s for 4 cycles) and sheared DNA fragments were ligated to custom-made MM76
582 and MM77 adapters[50]. Paired-end sequencing was performed on an Illumina sequencer
583 according to the manufacturer instructions (PairedEnd DNA sample Prep Kit – Illumina – PE-
584 930-1001). The custom-made adapters were removed from the reads using Cutadapt. Data
585 were then analysed using HiC-Pro[51]. Visualisation of contact-maps and computation of their
586 ratio was performed as described in[14]. We used custom MatLab functions to plot the 3C-seq
587 matrices (see Code availability).

588 # DATA AVAILABILITY

589 The NGS plasmid library verification, integration and excision data generated in this study have
590 been deposited in the NIH's Sequence Read Archive (SRA) database under accession code
591 GSM8423721, GSM8423722, GSM8423723, GSM8423724, GSM8423725, GSM8423726,
592 GSM8423727, GSM8423728, GSM8423729, GSM8423730, GSM8423731, GSM8423732,
593 GSM8423733, GSM8423734, GSM8423735, GSM8423736, GSM8423737, GSM8423738,
594 GSM8423739, GSM8423740, GSM8423741, GSM8423742, GSM8423743, GSE273190
595 GSM8423707, GSM8423708, GSM8423709, GSM8423710, GSM8423711, GSM8423712,
596 GSM8423713, GSM8423714, GSM8423715, GSM8423716, GSM8423717, GSM8423718,
597 GSM8423719, GSM8423720, GSE273189, GSM8423705, GSM8423706, GSE273188. For
598 microscopy images, representative datasets of raw images and all metadata generated in this

599 study have been deposited in the Mendeley public repository
600 (https://data.mendeley.com/datasets/782fzwyc2d/1). Considering the volume of imaging data
601 generated in this study, the remaining raw images are available from the corresponding author
602 within two weeks upon request. The data presented in Figure 3a-d, 4c-d, 5ed, 6a,
603 Supplementary Figure 5a and 6d are provided in the Supplementary Information/Source Data
604 file.

605 ## CODE AVAILABILITY

606 Custom MatLab functions used for analysing and plotting ChIP-seq, 3C-seq, Hi-SC2
607 and fluorescence microscopy results along with a set of example files are deposited in the
608 Zenodo public repository (https://zenodo.org, DOI 10.5281/zenodo.13236102).

609 ## REFERENCES

610 1. Bernhardt, T. G. & de Boer, P. A. SlmA, a nucleoid-associated, FtsZ binding protein required for
611 blocking septal ring assembly over Chromosomes in E. coli. *Mol Cell* **18**, 555–64 (2005).
612 2. Thanbichler, M. & Shapiro, L. MipZ, a spatial regulator coordinating chromosome segregation with
613 cell division in Caulobacter. *Cell* **126**, 147–162 (2006).
614 3. Wu, L. J. & Errington, J. Coordination of cell division and chromosome segregation by a nucleoid
615 occlusion protein in Bacillus subtilis. *Cell* **117**, 915–25 (2004).
616 4. Galli, E. *et al.* Cell division licensing in the multi-chromosomal Vibrio cholerae bacterium. *Nat.*
617 *Microbiol.* **1**, 16094 (2016).
618 5. Galli, E., Paly, E. & Barre, F.-X. Late assembly of the Vibrio cholerae cell division machinery
619 postpones septation to the last 10% of the cell cycle. *Sci. Rep.* **7**, (2017).
620 6. Adam, Y. *et al.* Plesiomonas shigelloides, an Atypical Enterobacterales with a Vibrio-Related
621 Secondary Chromosome. *Genome Biol. Evol.* **14**, evac011 (2022).
622 7. Galli, E. *et al.* Replication termination without a replication fork trap. *Sci. Rep.* **9**, 8315 (2019).
623 8. Val, M.-E. *et al.* FtsK-dependent dimer resolution on multiple chromosomes in the pathogen Vibrio
624 cholerae. *PLoS Genet.* **4**, e1000201 (2008).
625 9. David, A. *et al.* The two Cis-acting sites, parS1 and oriC1, contribute to the longitudinal organisation
626 of Vibrio cholerae chromosome I. *PLoS Genet.* **10**, e1004448 (2014).

627 10.Demarre, G. *et al.* Differential management of the replication terminus regions of the two Vibrio
628 cholerae chromosomes during cell division. *PLoS Genet.* **10**, e1004557 (2014).
629 11.Mercier, R. *et al.* The MatP/matS site-specific system organizes the terminus region of the E. coli
630 chromosome into a macrodomain. *Cell* **135**, 475–485 (2008).
631 12.Dupaigne, P. *et al.* Molecular basis for a protein-mediated DNA-bridging mechanism that functions
632 in condensation of the E. coli chromosome. *Mol. Cell* **48**, 560–571 (2012).
633 13.Seba, M., Boccard, F. & Duigou, S. Activity of MukBEF for chromosome management in E. coli and
634 its inhibition by MatP. *eLife* **12**, RP91185.
635 14.Lioy, V. S. *et al.* Multiscale Structuring of the E. coli Chromosome by Nucleoid-Associated and
636 Condensin Proteins. *Cell* **172**, 771-783.e18 (2018).
637 15.Espeli, O. *et al.* A MatP-divisome interaction coordinates chromosome segregation with cell division
638 in E. coli. *EMBO J.* **31**, 3198–3211 (2012).
639 16.Crozat, E. *et al.* Post-replicative pairing of sister ter regions in Escherichia coli involves multiple
640 activities of MatP. *Nat. Commun.* **11**, 3796 (2020).
641 17.Sadhir, I. & Murray, S. M. Mid-cell migration of the chromosomal terminus is coupled to origin
642 segregation in Escherichia coli. *Nat. Commun.* **14**, 7489 (2023).
643 18.Galli, E. & Gerdes, K. FtsZ-ZapA-ZapB interactome of Escherichia coli. *J. Bacteriol.* **194**, 292–302
644 (2012).
645 19.Männik, J., Castillo, D. E., Yang, D., Siopsis, G. & Männik, J. The role of MatP, ZapA and ZapB in
646 chromosomal organization and dynamics in Escherichia coli. *Nucleic Acids Res.* gkv1484 (2016)
647 doi:10.1093/nar/gkv1484.
648 20.Ozaki, S., Jenal, U. & Katayama, T. Novel Divisome-Associated Protein Spatially Coupling the Z-
649 Ring with the Chromosomal Replication Terminus in Caulobacter crescentus. *mBio* **11**, e00487-20
650 (2020).
651 21.Ozaki, S., Wakasugi, Y. & Katayama, T. Z-Ring-Associated Proteins Regulate Clustering of the
652 Replication Terminus-Binding Protein ZapT in Caulobacter crescentus. *mBio* **12**,
653 10.1128/mbio.02196-20 (2021).
654 22.Goudin, A., Ferat, J.-L., Possoz, C., Barre, F.-X. & Galli, E. Recovery of Vibrio cholerae polarized
655 cellular organization after exit from a non-proliferating spheroplast state. *PloS One* **18**, e0293276
656 (2023).

657 23. Yamaichi, Y., Fogel, M. A., McLeod, S. M., Hui, M. P. & Waldor, M. K. Distinct Centromere-Like parS
658 Sites on the Two Chromosomes of Vibrio spp. *J. Bacteriol.* **189**, 5314–5324 (2007).
659 24. Val, M.-E. *et al.* A checkpoint control orchestrates the replication of the two chromosomes of Vibrio
660 cholerae. *Sci. Adv.* **2**, e1501914–e1501914 (2016).
661 25. Bigot, S., Saleh, O. A., Cornet, F., Allemand, J.-F. & Barre, F.-X. Oriented loading of FtsK on KOPS.
662 *Nat. Struct. Mol. Biol.* **13**, 1026–1028 (2006).
663 26. Bigot, S. *et al.* KOPS: DNA motifs that control E. coli chromosome segregation by orienting the FtsK
664 translocase. *EMBO J.* **24**, 3770–3780 (2005).
665 27. Aussel, L. *et al.* FtsK Is a DNA motor protein that activates chromosome dimer resolution by switching
666 the catalytic state of the XerC and XerD recombinases. *Cell* **108**, 195–205 (2002).
667 28. Saleh, O. A., Pérals, C., Barre, F.-X. & Allemand, J.-F. Fast, DNA-sequence independent
668 translocation by FtsK in a single-molecule experiment. *EMBO J.* **23**, 2430–2439 (2004).
669 29. Val, M.-E., Skovgaard, O., Ducos-Galand, M., Bland, M. J. & Mazel, D. Genome Engineering in Vibrio
670 cholerae: A Feasible Approach to Address Biological Issues. *PLoS Genet.* **8**, (2012).
671 30. Nolivos, S. & Sherratt, D. The bacterial chromosome: architecture and action of bacterial SMC and
672 SMC-like complexes. *FEMS Microbiol. Rev.* **38**, 380–392 (2014).
673 31. Bürmann, F. *et al.* A folded conformation of MukBEF and cohesin. *Nat. Struct. Mol. Biol.* **26**, 227–
674 236 (2019).
675 32. Mäkelä, J. & Sherratt, D. J. Organization of the Escherichia coli Chromosome by a MukBEF Axial
676 Core. *Mol. Cell* **78**, 250-260.e5 (2020).
677 33. Mäkelä, J., Uphoff, S. & Sherratt, D. J. Nonrandom segregation of sister chromosomes by
678 *Escherichia coli* MukBEF. *Proc. Natl. Acad. Sci.* **118**, e2022078118 (2021).
679 34. Hayama, R. & Marians, K. J. Physical and functional interaction between the condensin MukB and
680 the decatenase topoisomerase IV in Escherichia coli. *Proc. Natl. Acad. Sci. U. S. A.* **107**, 18826–
681 18831 (2010).
682 35. Li, Y. *et al.* Escherichia coli condensin MukB stimulates topoisomerase IV activity by a direct physical
683 interaction. *Proc. Natl. Acad. Sci. U. S. A.* **107**, 18832–18837 (2010).
684 36. Fournes, F. *et al.* FtsK translocation permits discrimination between an endogenous and an imported
685 Xer/dif recombination complex. *Proc. Natl. Acad. Sci. U. S. A.* **113**, 7882–7887 (2016).

686 37. Crozat, E. *et al.* Separating speed and ability to displace roadblocks during DNA translocation by
687 FtsK. *EMBO J* **29**, 1423–33 (2010).
688 38. Adams, D. W., Wu, L. J. & Errington, J. Cell cycle regulation by the bacterial nucleoid. *Curr. Opin.*
689 *Microbiol.* **22**, 94–101 (2014).
690 39. Harrison, P. W., Lower, R. P. J., Kim, N. K. D. & Young, J. P. W. Introducing the bacterial 'chromid':
691 not a chromosome, not a plasmid. *Trends Microbiol.* **18**, 141–148 (2010).
692 40. Nielsen, H. J., Ottesen, J. R., Youngren, B., Austin, S. J. & Hansen, F. G. The Escherichia coli
693 chromosome is organized with the left and right chromosome arms in separate cell halves. *Mol.*
694 *Microbiol.* **62**, 331–338 (2006).
695 41. Lau, I. F. *et al.* Spatial and temporal organization of replicating Escherichia coli chromosomes. *Mol.*
696 *Microbiol.* **49**, 731–743 (2003).
697 42. Martin, M. Cutadapt removes adapter sequences from high-throughput sequencing reads.
698 *EMBnet.journal* **17**, 10–12 (2011).
699 43. Li, H. & Durbin, R. Fast and accurate long-read alignment with Burrows–Wheeler transform.
700 *Bioinformatics* **26**, 589–595 (2010).
701 44. Li, H. *et al.* The Sequence Alignment/Map format and SAMtools. *Bioinformatics* **25**, 2078–2079
702 (2009).
703 45. Sliusarenko, O., Heinritz, J., Emonet, T. & Jacobs-Wagner, C. High-throughput, subpixel precision
704 analysis of bacterial morphogenesis and intracellular spatio-temporal dynamics. *Mol. Microbiol.* **80**,
705 612–627 (2011).
706 46. Espinosa, E., Paly, E. & Barre, F.-X. High-Resolution Whole-Genome Analysis of Sister-Chromatid
707 Contacts. *Mol. Cell* **79**, 857-869.e3 (2020).
708 47. Sternberg, N. & Hamilton, D. Bacteriophage P1 site-specific recombination: I. Recombination
709 between loxP sites. *J. Mol. Biol.* **150**, 467–486 (1981).
710 48. Abremski, K., Hoess, R. & Sternberg, N. Studies on the properties of P1 site-specific recombination:
711 evidence for topologically unlinked products following recombination. *Cell* **32**, 1301–11. (1983).
712 49. Espinosa, E., Yamaichi, Y. & Barre, F.-X. Protocol for High-Throughput Analysis of Sister-Chromatids
713 Contacts. *STAR Protoc.* **1**, 100202 (2020).
714 50. Marbouty, M. *et al.* Metagenomic chromosome conformation capture (meta3C) unveils the diversity
715 of chromosome organization in microorganisms. *eLife* **3**, (2014).

716 51. Servant, N. *et al.* HiC-Pro: an optimized and flexible pipeline for Hi-C data processing. *Genome Biol.*
717 **16**, 259 (2015).

718 ACKNOWLEDGEMENTS

719 The work was supported by the Agence Nationale pour la Recherche [2018-CE12-0012-03
720 and 2023-CE12-0018-01 to F.-X.B., 2019-CE35-0013-01 to E.G.] and the Fondation pour la
721 Recherche Médicale [EQU202003010328 to F.-X.B.]. We thank E. Paly for helping in
722 constructing strains and plasmids, J. Provan, M. Seba, V. Lioy, S. Duigou, and Y. Yamaichi for
723 technical advice and helpful discussions.

724 AUTHOR CONTRIBUTIONS

725 J.-M. D. and C. P. performed the ChIP-seq experiments. F.-X. B. analysed ChIP-seq results.
726 M.-E. V., D. M., M. M. and R. K. performed and analysed the 3C-seq experiments. E. G.
727 performed and analysed the fluorescence microscopy observations. E.E. and J.C. performed
728 and analysed the Hi-SC2 experiments. E. G. and F.-X. B. supervised the work. All the authors
729 contributed to the writing.

730 COMPETING INTERESTS

731 The authors declare no conflict of interest.

732 FIGURE LEGENDS

733 **Fig. 1 | Numerous *matS* sites flank both *dif1* and *dif2*.**
734 **a** Schematic of newborn and dividing *V. cholerae* cells. Spiral line: flagellum; grey shading: cell
735 division proteins; blue and green gradients: SlmA-mediated nucleoid occlusion gradient; black
736 shaded circles: *ori1* and *ori2*; white shaded circles: *dif1* and *dif2*. By convention, the pole
737 resulting from the mother cell division is referred to as the new pole and the opposite pole,
738 where the flagellum is located, is referred to as the old pole. **b** *V. cholerae* chromosome maps.
739 ChrI and ChrII are depicted in blue and green, respectively. Black rectangles: super integron
740 (SI), Vibrio Pathogenicity Islands (VPI1, VPI2), Vibrio Seventh pandemic Islands (VSP1,
741 VSP2) and O-antigen cluster (Oanti), as indicated. The position of *crtS* and of the loci tagged

742 for microscopic observation are indicated. **c** ChIP-seq analysis of the binding of *V. cholerae*
743 MatP. Blue and green lines: relative sequence enrichment profiles along ChrI and ChrII,
744 respectively. The profiles were smoothed using a sliding average distance of 100 bp and scaled
745 between 0 (lowest enrichment locus along the whole genome) and 1 (highest enrichment locus
746 over the whole genome, indicated with a star). The MEME logos of the *matS* sites found on
747 ChrI and ChrII are shown above their respective profiles. The position weight matrix of the
748 ChrII sites matches that of the ChrI sites (Two-sided Pearson correlation, p-value: 1.95E-11,
749 q-value: 3.89E-11). Genomic features of interest are displayed on the x-axis. Black dotted lines
750 indicate the boundaries of the *TerI* and *TerII* MDs. **d** Relative enrichment of the sequences as
751 a function of their MCAST score. Blue and Red: N16961 *V. cholerae matS* sites bound and not
752 bound by MatP, respectively. A star indicates the motif showing the highest enrichment. **e** 40
753 kbp sliding average profile of the number of *matS* sites along ChrI and ChrII indicating the
754 expected enrichment of MatP-bound sequences at the centre of *TerI* and *TerII* induced by the
755 local density of *matS* sites. **f** 40 kbp sliding average profile of Fig. 1c ChIP-seq data, showing
756 the actual enrichment of MatP at the centre of *TerI* and *TerII*. Genomic features of interest are
757 displayed on the x-axis.

758 **Fig. 2 | MatP structures *TerI* and *TerII* into macrodomains.**

759 Ratio plot of the 3C-seq maps of Δ*matP* and *matP*$^+$ cells. A decrease or increase in contacts
760 in 5-kbp bins in Δ*matP* cells compared with *matP*$^+$ cells is represented with a blue or red colour,
761 respectively. White indicates no differences between the two conditions. Genomic features of
762 interest are indicated on the bottom and left axes. The ChIP-seq profile obtained with the
763 *matP3flag* allele is shown on the top and right axes. Black dotted lines indicate the boundaries
764 of the *TerI* and *TerII* MDs.

765 **Fig. 3 | MatP increases cohesion in the immediate vicinity of *dif1* and *dif2*.**

766 **a** Relative longitudinal axis position of single spots. The new and old pole positions are set to
767 0 and 1, respectively. Results correspond to a median number of 591 cells for each locus
768 (Supplementary Data 3). **b** Relative distance along the longitudinal axis between sister copies
769 of each tagged locus in old cells. Results correspond to a median number of 319 cells for each

770 locus (Supplementary Data 3). The median (disk), first and third quartile (horizontal marks) of
771 the positions/sister distances are shown for each tagged locus. Solid lines: expected
772 position/sister distance of intermediate loci; Dashed lines: the expected symmetrical
773 position/sister distance of loci on the left replication arm of ChrI; Blue and pink: ChrI; green
774 and orange: ChrII; blue and green: *matP*$^+$ cells (WT); pink and orange: Δ*matP* cells (Δ*matP*);
775 Arrows: *TerI* and *TerII* MDs. Genomic features of interest are displayed on the x-axis. **c** log2 of
776 the spot duplication frequency at each locus (blue, pink, green and orange lines) and increase
777 in duplication frequency at each locus in Δ*matP* cells (grey bars). **d** Cre/*loxP*-based Hi-SC2
778 analysis of the relative frequency of contacts of newly-replicated copies behind replication
779 forks. **e** FtsK/XerCD/*dif1*-based Hi-SC2 analysis of the relative frequency of contacts of sister
780 copies during septum closure. Results are shown at a 40 kbp resolution. Black dotted lines
781 indicate the zones where sister chromatid contacts are less frequent in Δ*matP* cells than in WT
782 cells. Grey surfaces highlight the global reduction of sister chromatid contacts in these zones.
783 Genomic features of interest are displayed on the x-axis. The corresponding percentages of
784 reduction is indicated. Hi-SC2 analysis replicates are shown in Supplementary Fig. 5b,c.
785 Source data of panel a, b and c are provided as a Source Data file.

786 **Fig. 4 | MatP increases cohesion in highly enriched *matS* regions.**

787 **a** MCH1 chromosome map. Regions originating from ChrI and ChrII are depicted in blue and
788 green, respectively. *ori1*, *dif2*, SI, VPI1, VPI2, VSP1, VSP2, O-antigen cluster, *crtS* and
789 positions of the loci tagged for microscopic observation are indicated as in Fig. 1. **b** ChIP-seq
790 analysis of the binding of *V. cholerae* MatP in MCH1. Relative sequence enrichment profile
791 along MCH1 genome (100 bp sliding average). The profile was scaled between 0 (lowest
792 enrichment locus along the whole genome) and 1 (highest enrichment locus over the whole
793 genome, indicated with a star). Genomic features of interest are displayed on the x-axis. **c**
794 Relative longitudinal axis position of each tagged locus in young cells. Results correspond to
795 a median number of 638 cells for each locus. **d** Relative distance along the longitudinal axis of
796 sister copies of each tagged locus in old cells. Results correspond to a median number of 417
797 cells for each locus (Supplementary Data 3). The median (disk), first and third quartile

798 (horizontal marks) of the positions/sister distances are shown for each tagged locus. Solid
799 lines: expected position/sister distance of intermediate loci; Dashed lines: the expected
800 symmetrical position/sister distance of loci on the left replication arm; Blue and pink: regions
801 originating from ChrI; green and orange: regions originating from ChrII; blue and green: *matP*$^+$
802 cells (MCH1); pink and orange: Δ*matP* cells (MCH1 Δ*matP*); Arrows: limits of Left, Ter and
803 Right MDs. Genomic features of interest are displayed on the x-axis. **e** log2 of the spot
804 duplication frequency at each locus (blue, pink, green and orange lines) and increase in
805 duplication frequency at each locus in MCH1 Δ*matP* cells (grey bars). **f** Cre/*loxP*-based Hi-
806 SC2 analysis of the relative frequency of contacts of newly-replicated copies behind replication
807 forks. **g** FtsK/XerCD/*dif1*-based Hi-SC2 analysis of the relative frequency of contacts of sister
808 copies during septum closure. Results are shown at a 40 kbp resolution. Black dotted lines
809 indicate the zones where sister chromatid contacts are less frequent in MCH1 Δ*matP* cells
810 than in MCH1 cells. Grey surfaces highlight the global reduction of sister chromatid contacts
811 in these zones. Genomic features of interest are displayed on the x-axis. The corresponding
812 percentage of reduction is indicated. Hi-SC2 analysis replicates are shown in Supplementary
813 Fig. 6e and 6f. Source data of panels c, d and e are provided as a Source Data file.

814 **Fig. 5 | MatP action depends on the number and local density of *matS* sites.**

815 **a** and **f** JVV024 and EPV487 chromosome maps, respectively. ChrI and ChrII are depicted in
816 blue and green, respectively. The position of the *matS* sites on JVV024 ChrI and ChrII are
817 indicated by pink and orange triangles, respectively. The two *matS* sites that were deleted from
818 JVV024 ChrI and inserted in ChrII are depicted by white and pink triangles with a black contour,
819 respectively. The inverted region in EPV487 *TerI* is highlighted in red. Genomic features of
820 interest are indicated as in Fig. 1b. **b** and **g** ChIP-seq analysis of the binding of *V. cholerae*
821 MatP in JVV024 and EPV487, respectively. The 100 bp and 40 kbp sliding average profiles
822 are shown to indicate the *matS* sites and to highlight the enrichment of MatP in *TerI* and *TerII*.
823 Genomic features of interest are displayed on the x-axis. **c** and **h** FtsK/XerCD/*dif1*-based Hi-
824 SC2 analysis of the relative frequency of contacts of sister copies during septum closure in
825 JVV024 and EPV487, respectively. Results are shown at a 40 kbp resolution. Genomic

826 features of interest are displayed on the x-axis. **d** Distance along the longitudinal axis between
827 sister copies of DI and DII spots. The median (horizontal bar), the 25th and the 75th percentiles
828 (open box) and the 5th and the 95th percentiles (error bars) of the sister spot distances are
829 represented for each sample. Results correspond to 4 (N16961) and 3 (JJV024 and EPV487)
830 biological replicates, with a median number of 254 cells per strain per replicate (Supplementary
831 Data 3). ** and n.s.**:** significantly and not significantly different, respectively (Wilcoxon-Mann-
832 Whitney test, Supplementary Table 1). **e** Cells were classified in four categories as a function
833 of the number of DI and DII spots (1 DI & 1 DII spots, 2 DI &1 DII spots, 1 DI & 2 DII spots,
834 and 2 DI & 2 DII spots) and the ratio of cells from the second category over the number of cells
835 from the second and third categories (mean and SD). Results correspond to 4 (N16961) and
836 3 (JJV024 and EPV487) biological replicates, with a median number of 3031 cells per strain
837 per replicate (Supplementary Data 3). ** and n.s.**:** significantly and not significantly different,
838 respectively (Wilcoxon-Mann-Whitney test, Supplementary Table 2). Source data of panel d
839 and e are provided as a Source Data file.

840 **Fig. 6 | MatP acts independently of cell division and tetramer formation.**

841 **a** Relative distance between sister copies of the DI (blue) and DII (green) locus. The median
842 (horizontal bar), the 25th and the 75th percentiles (open box) and the 5th and the 95th
843 percentiles (error bars) of the sister spot distances are represented for each sample. Dotted
844 lines highlight the median DI (blue) and DII (green) sister spot distance in WT cells. A median
845 number of 225 cells were analysed for qeach strain (Supplementary data 3). ** and n.s.**:**
846 significantly and not significantly different, respectively (Wilcoxon-Mann-Whitney test,
847 Supplementary Table 3). Source data are provided as a Source Data file. **b** Cellular localisation
848 of DI foci over-time in time-lapse experiments of WT and mutant *V. cholerae* strains. Each
849 panel shows the compilation of individual traces. In the heat maps, black corresponds to the
850 lowest and dark red to the highest intensities. y-axis: position along the cell length, with 0
851 corresponding to the new pole and 1 to the old pole. x-axis: relative advancement of the cell
852 cycle from the first image observed after birth and the last image before division. **c** Cellular
853 localisation of DI foci over-time in time-lapse experiments in *ftsZ84*^{ts} and *ftsZ84*^{ts} Δ*matP* cells

854 grown at 42°C. On the top-right corner of each frame is indicated the time in minutes from the

855 beginning of imaging. Scale bar = 2 μm.

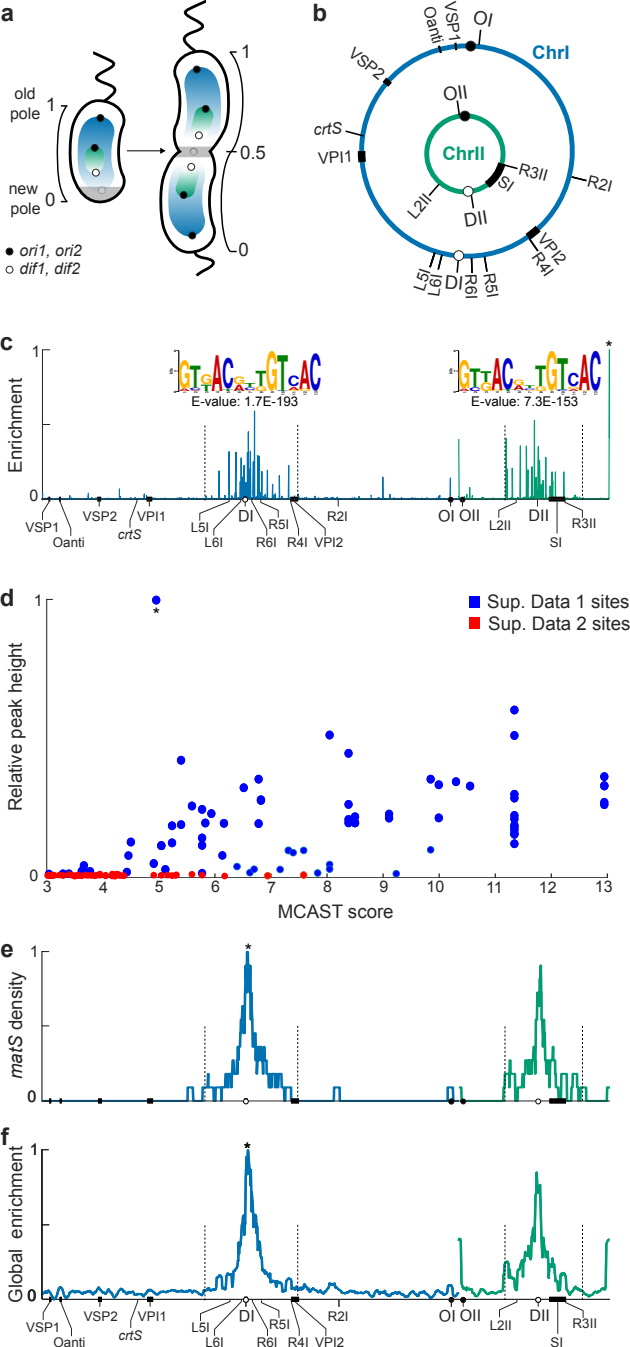
a
old pole
new pole
1
0
1
0.5
0
● ori1, ori2
○ dif1, dif2
b
ChrI
ChrII
OI
VSP1
Oanti
VSP2
crtS
VPI1
OII
DII
SI
R3II
R2I
VPI2
R4I
R5I
R6I
DI
L5I
L6I
L2II
c
Enrichment
E-value: 1.7E-193
E-value: 7.3E-153
VSP1
Oanti
VSP2
crtS
VPI1
L5I
L6I
DI
R5I
R6I
R4I
VPI2
R2I
OI
OII
L2II
DII
SI
R3II
d
Relative peak height
MCAST score
Sup. Data 1 sites
Sup. Data 2 sites
e
matS density
f
Global enrichment

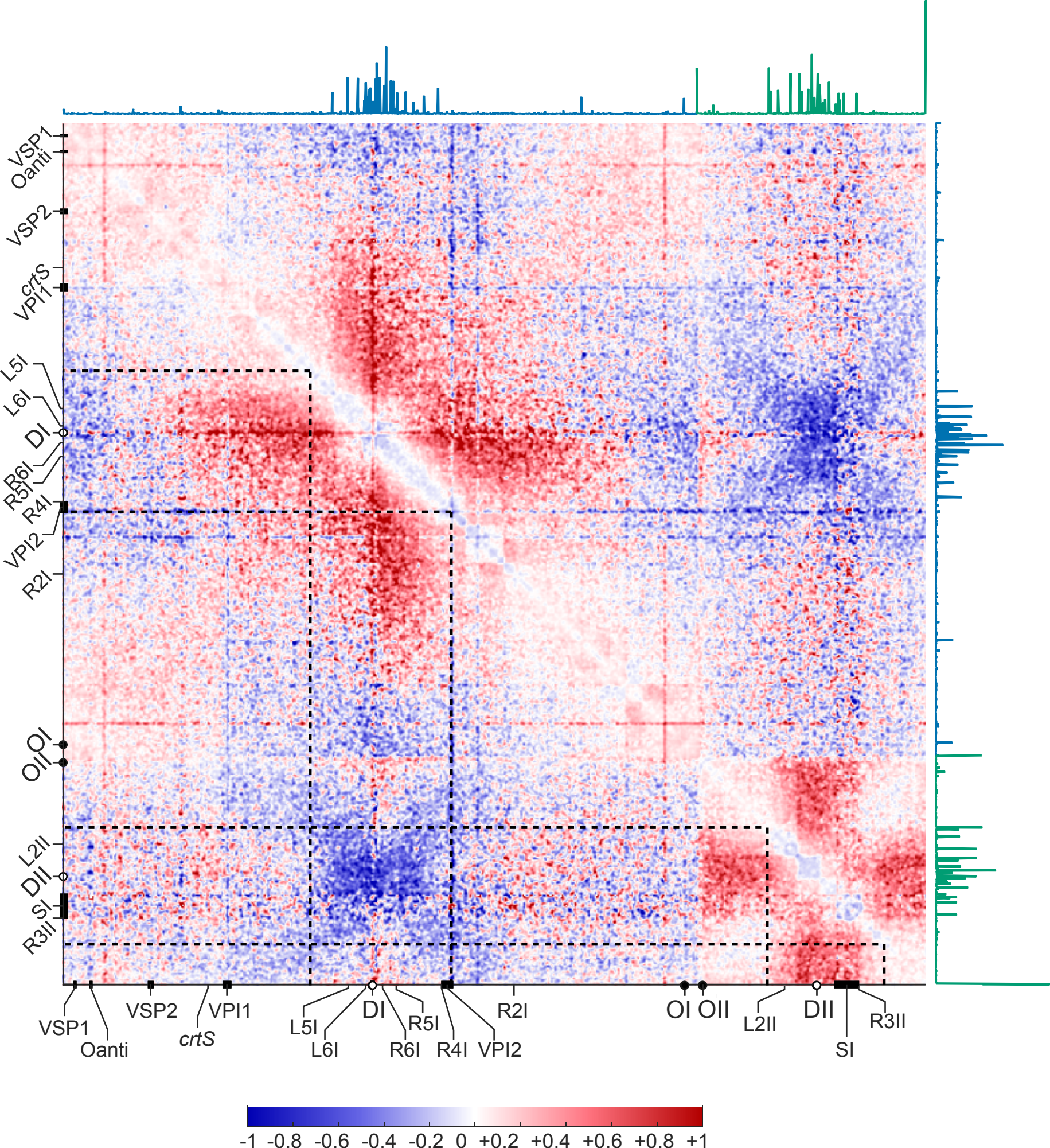
VSP1
Oanti
VSP2
crtS
VPI1
L5I
L6I
DI
R6I
R5I
R4I
VPI2
R2I
OI
OII
L2II
DII
SI
R3II
VSP1
Oanti
VSP2
crtS
VPI1
L5I
L6I
DI
R6I
R5I
R4I
VPI2
R2I
OI
OII
L2II
DII
SI
R3II
-1 -0.8 -0.6 -0.4 -0.2 0 +0.2 +0.4 +0.6 +0.8 +1

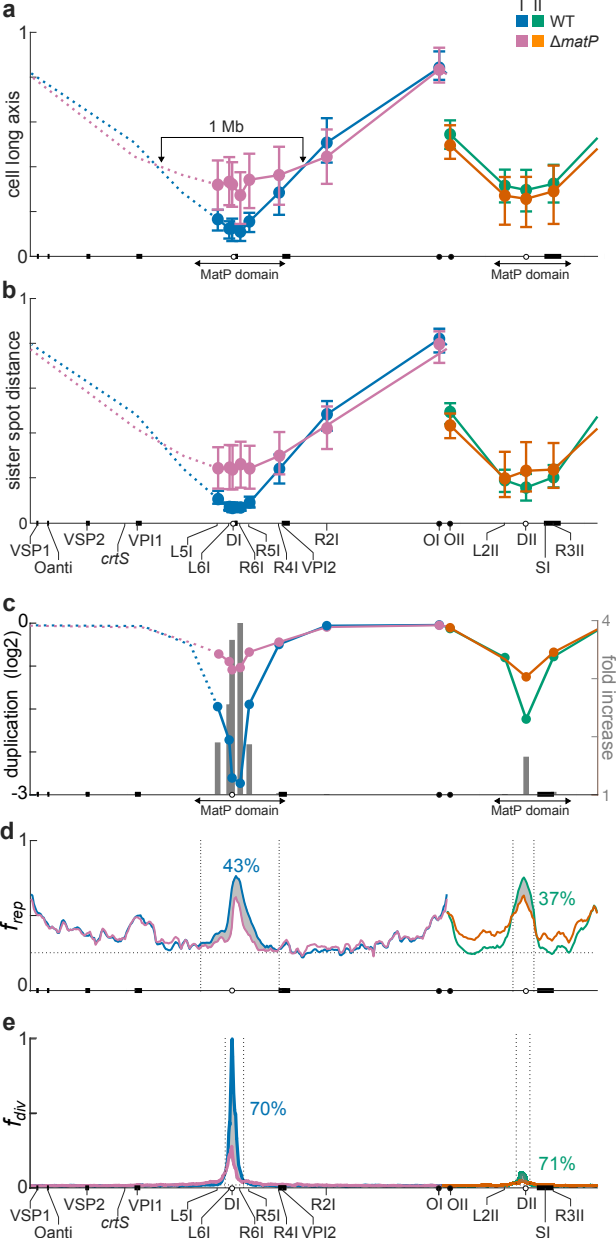
a
I II
WT
ΔmatP
cell long axis
1 Mb
MatP domain
MatP domain
b
sister spot distance
VSP1
Oanti
VSP2
crtS
VPI1
L5I
L6I
DI
R6I
R5I
R4I
R2I
VPI2
OI OII
L2II
DII
SI
R3II
c
duplication (log2)
fold increase
MatP domain
MatP domain
d
f_{rep}
43%
37%
e
f_{div}
70%
71%
VSP1
Oanti
VSP2
crtS
VPI1
L5I
L6I
DI
R6I
R5I
R4I
R2I
VPI2
OI OII
L2II
DII
SI
R3II

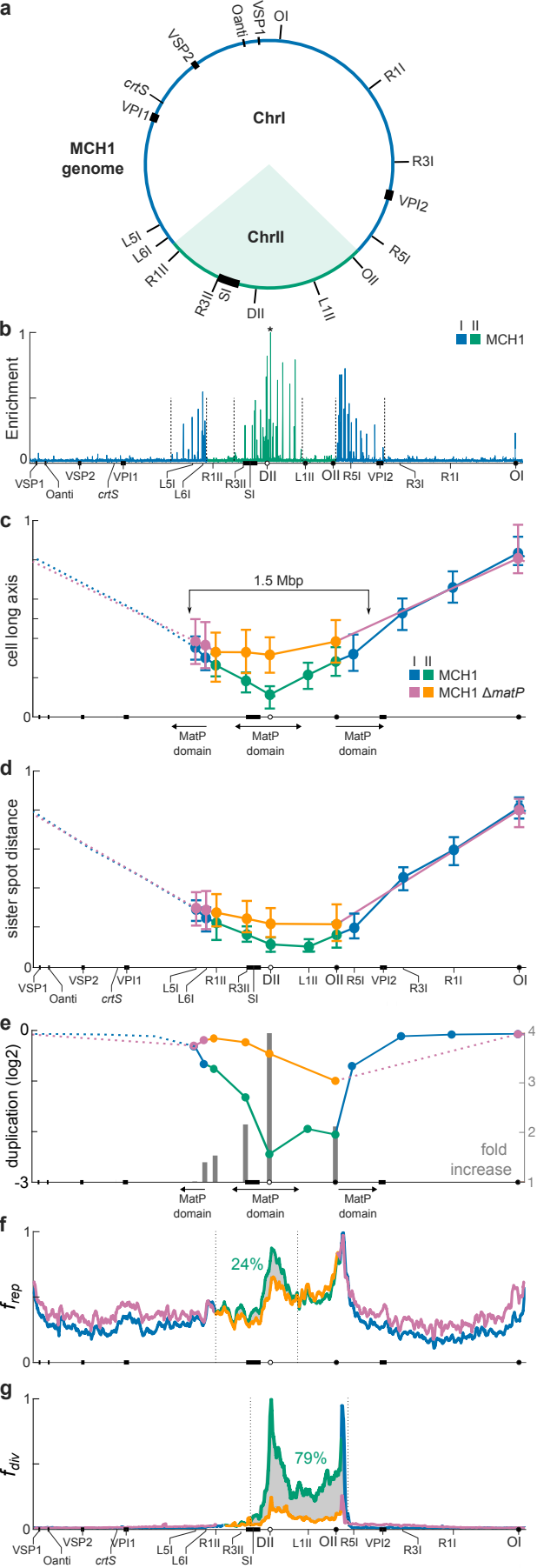
a
MCH1 genome
ChrI
ChrII
Oanti
VSP1
OI
VSP2
R1I
crtS
VPI1
R3I
VPI2
L5I
L6I
R5I
R1II
OII
R3II
SI
DII
L1II
b
Enrichment
I II
MCH1
VSP1
Oanti
VSP2
crtS
VPI1
L5I
L6I
R1II
R3II
SI
DII
L1II
OII
R5I
VPI2
R3I
R1I
OI
c
cell long axis
1.5 Mbp
I II
MCH1
MCH1 ΔmatP
MatP domain
MatP domain
MatP domain
d
sister spot distance
e
duplication (log2)
fold increase
MatP domain
MatP domain
MatP domain
f
f_{rep}
24%
g
f_{div}
79%

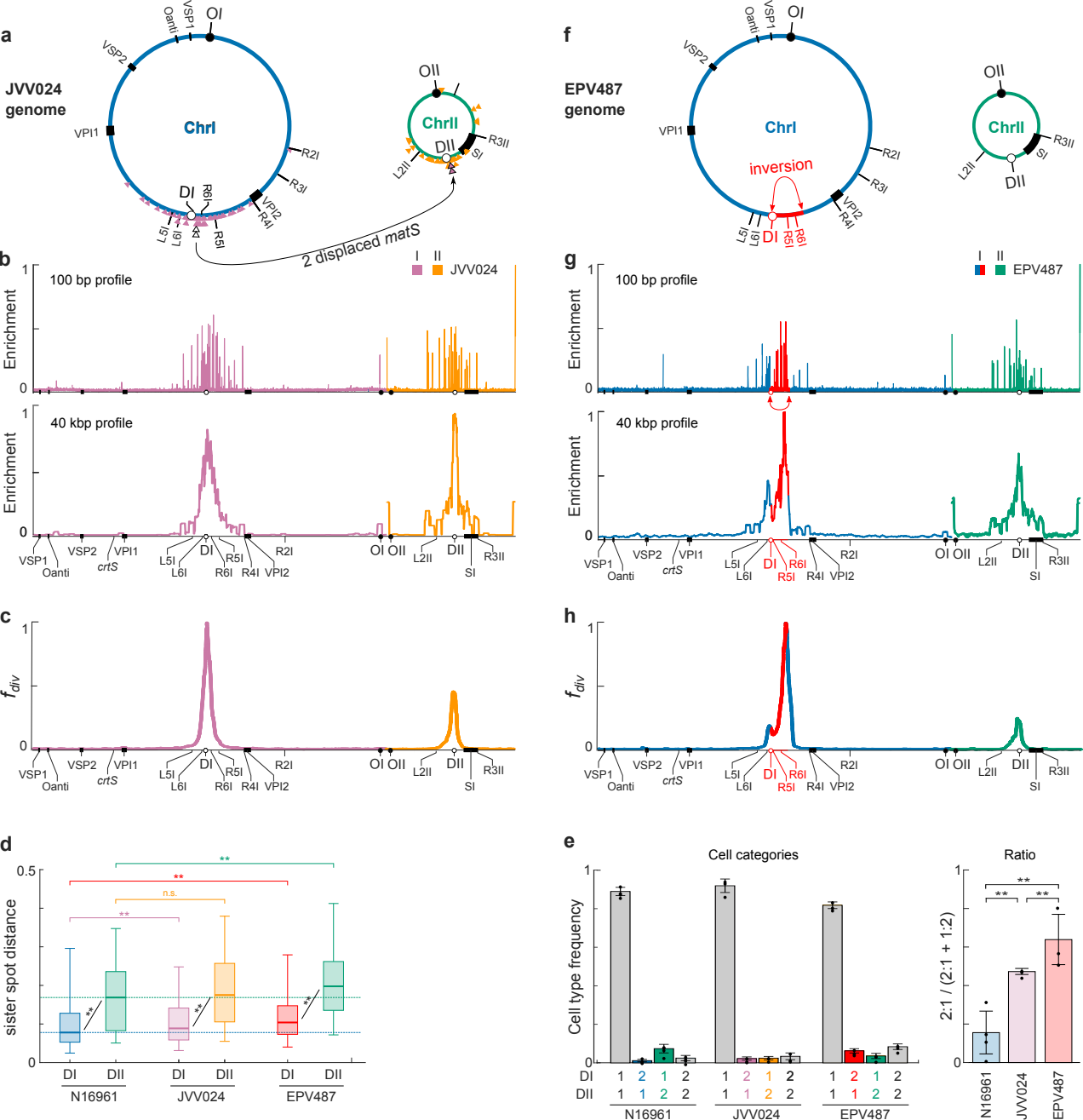
a
JVV024 genome
ChrI
ChrII
OI
OII
DI
DII
2 displaced matS
b
100 bp profile
40 kbp profile
Enrichment
JVV024
c
f_{div}
d
sister spot distance
N16961
JVV024
EPV487
f
EPV487 genome
inversion
g
h
e
Cell categories
Cell type frequency
Ratio
2:1 / (2:1 + 1:2)

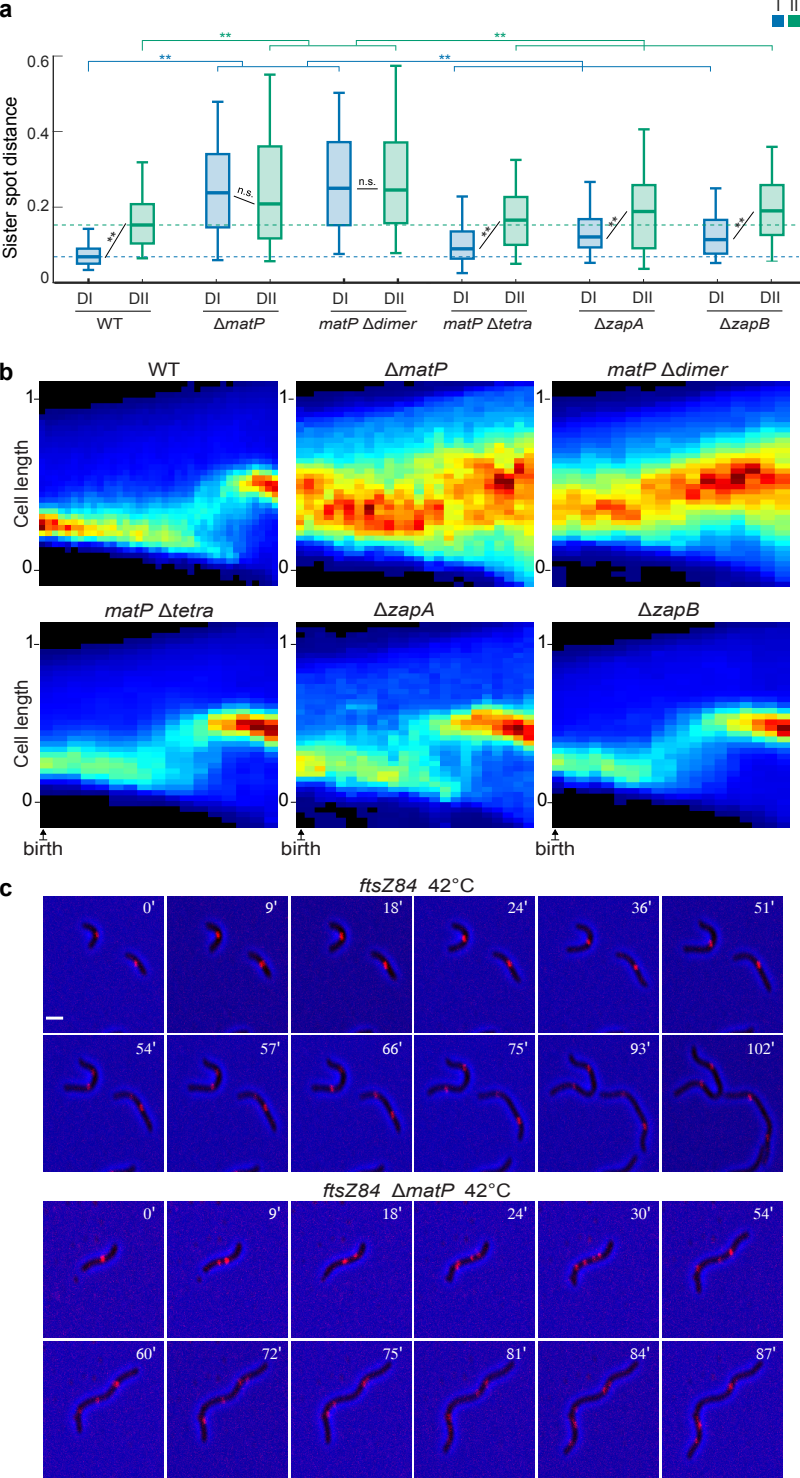
a
I
II
Sister spot distance
0.6
0.4
0.2
0
**
n.s.
DI
DII
WT
ΔmatP
matP Δdimer
matP Δtetra
ΔzapA
ΔzapB
b
Cell length
1
0
birth
c
ftsZ84 42°C
0'
9'
18'
24'
36'
51'
54'
57'
66'
75'
93'
102'
ftsZ84 ΔmatP 42°C
30'
60'
72'
81'
84'
87'